communications materials

ARTICLE

https://doi.org/10.1038/s43246-024-00446-y OPEN

Transient co-tuning of atomic Fe and nanoparticle facets for self-relaying Fenton-like catalysis

Jiewen Luo[1,2], Xiangdong Zhu[3✉], Fengbo Yu[3], Chao Jia[3], Chao Liu[1], Qing Zhao[1,2], Xiaoli Zhao[1,2,4✉] & Fengchang Wu[1,2,4✉]

Fenton-like catalysts are important materials for degrading refractory organic pollutants, however, they still suffer from limited oxidizing ability. Although single atoms and nanoparticles with high-index facets are commonly used in catalysis, their high surface energy hinders controllable synthesis. Here, we construct an iron-based material containing both isolated single atoms and high-index faceted nanoparticles by carbon-assisted Flash Joule heating for organic pollutant remediation. The current-induced thermal shock benefits the excitation of iron atoms and subsequent trapping by graphene defects. At ultrahigh temperatures, the thermodynamic limitations are overcome, leading to nanoparticles with high-index facets. Density functional theory calculations indicate that hydroxyl radical production can be enhanced by self-relay catalysis via the ensemble effect between single atoms and high-index facet nanoparticles. The derived materials exhibit dramatically improved performance in terms of antibiotic removal and medical micropolluted water. Thus, this method presents an effective strategy for designing smart materials for organic wastewater purification.

[1] Guangdong Key Laboratory of Integrated Agro-environmental Pollution Control and Management, Institute of Eco-environmental and Soil Sciences, Guangdong Academy of Sciences, Guangzhou, China. [2] National-Regional Joint Engineering Research Center for Soil Pollution Control and Remediation in South China, Guangzhou, China. [3] Department of Environmental Science and Engineering, Fudan University, Shanghai, China. [4] State Key Laboratory of Environmental Criteria and Risk Assessment, Chinese Research Academy of Environmental Sciences, Beijing, China. ✉email: zxdjewett@fudan.edu.cn; zhaoxiaoli_zxl@126.com; wufengchang@vip.skleg.cn

Nanomaterial ensembles consisting of single metal atoms and nanoparticles have garnered significant attention due to their ability to increase the rate of advanced oxidation processes[1–3]. It is critical to tailor the active sites with high surface energy and reactivity properties, as this sites can overcome the limitations of conventional degradation processes with respect to their kinetics and activities[4,5]. This tailoring supports the development of better materials for treating refractory organic pollutants.

In particular, single atoms and high-index facet nanoparticles are important classes for electron transfer modulation[6–10], and drive the adsorption of reaction intermediates (such as $SO_4^{\cdot-}$ and $S_2O_8^{2-}$), reduce the energy barrier and facilitate the rate-limiting step[11–13]. Single atom sites have rich and uniform coordination structures[14,15], leading to more opportunities for adsorbing oxygen-containing species and optimizing the binding energy of oxidant intermediates. Due to the lack of metal–metal bonds, single atom materials lack electronic synergy among metal active sites, resulting in subtle electronic effects and hindering the rate–determining step[16]. In this case, high-index faceted nanoparticles possess high densities of low–coordination atoms, steps, edges, and junctions in these structures[17], which exist as active auxiliaries and compensate for the shortage of single atoms. These nanoparticles can accelerate charge transfer and trigger a combined effect with single atoms to overcome limitations in the activity capacity. Thus, multiple types of active sites can coordinate catalytic functions in oxidation reactions, thereby effectively performing self-relay catalysis and achieving more efficient and selective oxidation processes[18,19]. However, there are few effective methods for controlling structures because of the simultaneous presence of high-surface energy active sites. Both of these active sites are not stable during synthesis due to their high surface energies. On the one hand, single atoms usually possess relatively high mobility, and are inclined to agglomerate into thermodynamically stable particles via Ostwald ripening[20]. On the other hand, the organic ligands that stabilize high-index facets usually decompose upon thermal annealing, easily reconstructing their facets into low-index facets.

To meet this challenge, carbon-assisted flash Joule heating (C-FJH) has been reported to be a facile synthesis method[21–24], that is promising for material design processes. This reaction involves the rapid heating of a material using an electric current, and the duration of the reaction is typically very short, on the order of seconds, which allows for the very rapid heating and cooling of the material. The current induces a thermal shock duration that is beneficial for the excitation of metal atoms and the trapping of carbon matrix defects, further preventing extended heat-induced atom aggregation[25,26]. Additionally, the C-FJH process can be used to induce controlled sintering of metal nanoparticles, which can help increase the size and stability of high-index facets. The ultrahigh temperature overcomes thermodynamic limitations and synthesizes nanoparticles with high-index facets; the quenching process causes facet coagulation and circumvents reconstruction into low-index facets. Moreover, high-temperature carbothermal reduction can induce the formation of various valence states and vacancy defects on the surface, changing the electronic structure and ultimately influencing the reactivity and selectivity of the material.

Herein, we used the C-FJH method to synthesize a highly effective Fe-based material. The material contains isolated single atoms and high-index faceted nanoparticles on the graphene structure. Experiments and density functional theory (DFT) calculations showed that the combination of both active sites led to superior activity during persulfate (PDS) activation for antibiotic removal and for medical micropolluted water treatment. These results demonstrate the promising potential of this material for special designs and for high-performance organic pollutant remediation.

Results and discussion

Carbon-assisted Flash Joule heating induces Fe single-atom and high-index faceted nanoparticles. A schematic diagram of the synthesis of Fe-based materials by the reformative C-FJH method is shown in Supplementary Fig. 1. In the C-FJH process, electrothermal energy is provided to the reactants within one second (initial stage) using capacitor banks in the circuit (Fig. 1a), bringing the sample precursor to an ultrahigh temperature. The current-induced thermal shock benefits the excitation of Fe atoms and enhances the homogeneous reactions between the metal precursor and the amorphous carbon source to form atomic Fe, which is subsequently trapped by defects in graphene (Fig. 1b). Additionally, the ultrahigh temperature (~2500 K, Fig. 1c) required to overcome the thermodynamic limitation is conducive to synthesizing nanoparticles with high-index facets; this rapid quenching process causes facet coagulation. This phenomenon allows the coexistence of high surface energy active sites that are difficult to prepare using traditional methods (Fig. 1b). Inspired by the superior degradation performance of the C-FJH derived material (named FJH-Fe-G, Fig. 1d), the final chloramphenicol (CAP) degradation efficiencies of HY-Fe-C (derived from the hydrothermal-coprecipitation method), PY-Fe-C (derived from traditional pyrolysis method) and FJH-Fe-G materials were at approximately 18.7%, 12.8% and 93.0%, respectively. Notably, these materials show limited adsorption capacities (Supplementary Fig. 2), which are probably restricted by their limited porosity and surface area (Supplementary Table 1). The second-order rate constant (k_{obs}) of the C-FJH material is 22.7 $mmol^{-1}$/h, which is twoorders of magnitude greater than that of the HY-Fe-C (0.50 $mmol^{-1}$/h) and PY-Fe-C (0.22 $mmol^{-1}$/h) materials (Supplementary Fig. 3). This impressive catalytic performance surpasses that of many reported Fe-based Fenton-like materials (Fig. 1e and Supplementary Table 2). Thus, we doubted that the C-FJH effect dominates the features of the derived materials, forming built-up active sites.

First, we explored the structures of the C-FJH materials to evaluate the outstanding properties of the technical course. Scanning transmission electron microscopy (STEM) images (Fig. 2a, b), show that thermal shock overcomes the energy barrier of metal atomization, decreases the size of Fe nanoparticles and transforms nanoparticles into single atoms (Fig. 2a). Elemental mapping verified the homogeneous distribution of Fe and the uniform sizes of the atoms that were present on the carbon support (Fig. 2a and Supplementary Fig. 4). Some of the atoms assembled into Fe nanoparticles are influenced by atomic interactions[27], and the graphene structure can be utilized as an isolator to spatially separate metal sites by forming a protective layer around them (Fig. 2b). The exfoliation effect converts nanosheets into a graphene structure (Supplementary Fig. 5), which contributes to the enhanced structural stability of the anchored atomic Fe and nanoparticles. As confirmed by the Raman results (Supplementary Fig. 6, calculated from the integral area of the characteristic peaks), the C-FJH-derived material exhibited a lower I_D/I_G ratio (0.36) and a high 2D bank at a low $I_{2D/G}$ value (0.49). This smooth surface of the nanosheet favors more efficient exposure of atomic-level active sites. Conversely, hydrothermal-coprecipitation method-derived and pyrolysis method-derived Fe-based materials are fabricated over hundreds of nanometers with rod-like (HY-Fe-C) and bulk-like (PY-Fe-C) features, respectively (Supplementary Fig. 7).

Additionally, decreasing the particle size (average of ~11 nm) induces extrusion of the lattice (Supplementary Fig. 8),

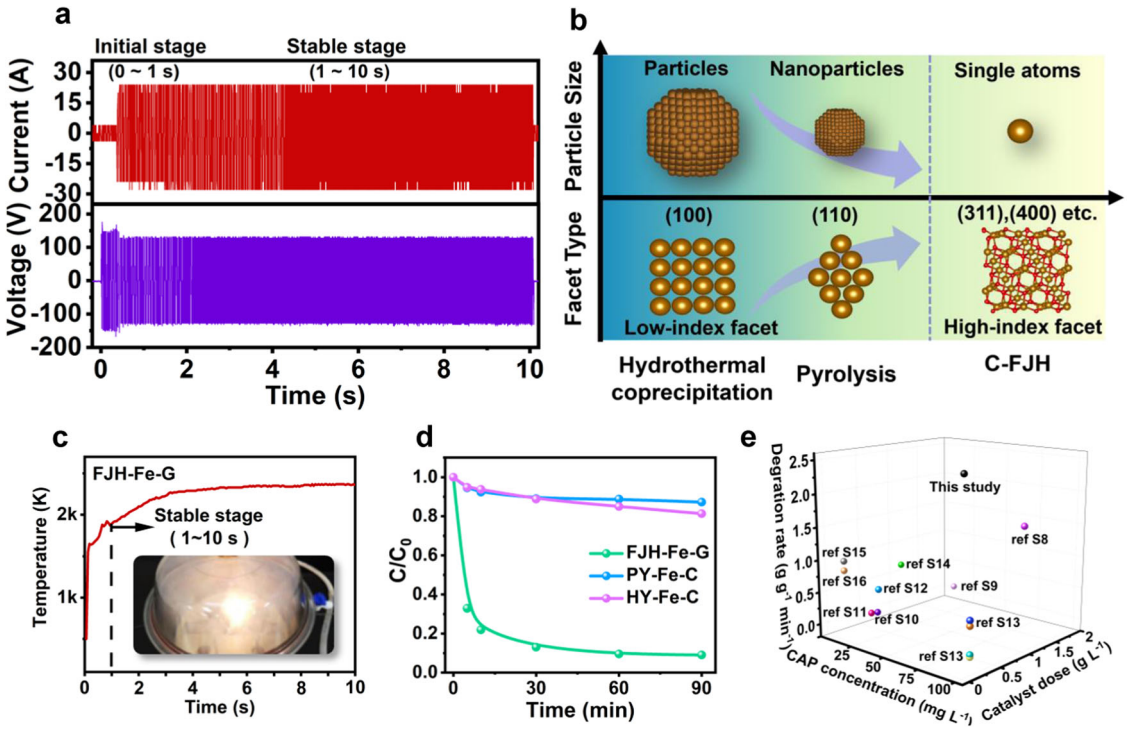

Fig. 1 Overview of dual active sites material from C-FJH method. a Schematic showing the synthesis of ensembles with atomic Fe and high-index facet nanoparticle materials by the C-FJH method. **b** Current and voltage changes in the C-FJH process. **c** Temperature change during the C-FJH process. **d** CAP degradation profiles of the prepared material (reaction conditions: the concentrations of CAP, PDS, and the material were 80 mg L^{-1}, 5 mmol L^{-1}, and 0.5 g L^{-1}, respectively). **e** Comparison of the CAP removal rate per gram of material per minute (g g^{-1} min^{-1} C) between the materials in the reference and the C-FJH-derived material (references listed in Table S5).

dominating the narrow lattice distances of the crystal facets and resulting in high-index facet attainment. High-resolution transmission electron microscopy (HRTEM) images of the C-FJH-derived material exhibit an interplanar lattice spacing of 0.19 nm, which is in good agreement with that of Fe_3O_4 (311) (Fig. 2c). A high-index facet is observed for Fe (211) in the electron diffraction pattern (Fig. 2c), and Fe_3O_4 (400) and (511) are observed in the X-ray diffraction (XRD) pattern (Supplementary Fig. 9). Fe and Fe_3O_4 particles are the main nanoparticle components on the material surface. As confirmed by ^{57}Fe Mössbauer spectra (Supplementary Fig. 10), α-Fe (36.7%), Fe_3O_4 (5.3%), Fe^{2+} (Fe_5C_2) and discorded Fe–O(C) (31.5%) coexisted in the FJH-Fe-G sample (Supplementary Table 3). In addition, a double doublet corresponding to Fe single atom coordination structure was observed (26.4%). In addition, some lattice defects (vacancies) and lattice distortions from the lattice fringes of nanoparticles (e.g., Fe_3O_4) are observed (Fig. 2d). Typically, the surface areas of high-energy facets decrease and eventually disappear during morphological evolution. For example, the resultant HY-Fe-C and PY-Fe-C materials are related to FeOOH and Fe_2O_3 (Supplementary Fig. 9), with dominant fates of (110), (120), and (111) (Fig. 2e). This finding implies that the rapid quenching in C-FJH prevents the degradation of facets into low-index facets by increasing the growth rate. However, Fe_3O_4 (311) is thermodynamically stable and preferentially preserved at a surface energy of 0.028 eV/Å^2 (0.44 J/m^2) (Fig. 2f). The C-FJH process promotes the formation of high-index facets and Fe_3O_4 (311) facets, which contain vacancies that have more unsaturated surface sites. Furthermore, we identified the major reactive sites of Fe (including Fe^0 and Fe^{2+}) on various materials. The FJH-Fe-G material showed distinct peaks corresponding to Fe^0 and Fe^{2+} (Supplementary Fig. 11a), with maximum Fe^0 and Fe^{2+}/Fe_{total} ratios (Supplementary Table 4, calculated by the fitting peak areas). In addition, the peak intensity of surface chemisorbed O^{2-} species can proportionally reflect the number of surface oxygen vacancies[28]. Clearly, the peak intensity of O^{2-} species slightly increased in FJH-Fe-G, indicating an increased number of surface oxygen vacancies (Supplementary Fig. 11b). Joule heating provides a transient high temperature that induces strong carbon thermal reduction, transforming Fe into a reduced valence state. These finding indicate the successful engineering of the Fe valence state (Fe^0 and Fe^{2+}) during the C-FJH process for optimizing active sites.

Specifically, the atomic local structure of the FJH-Fe-G material was determined by fine structure measurements via X-ray absorption[29]. Like in the above results, the valence of Fe in the FJH-Fe-G material is between 0 and +2, according to the rising edge between the Fe foil and FeO (Supplementary Fig. 12). The Fourier transform (FT) k^3-weighted curve of the extended X-ray absorption fine structure curve for the FJH-Fe-G material displays two main peaks at ~1.5 (Fe-O) and ~2.2 Å (Fe-Fe) (Fig. 2g). According to the wavelet transform (WT) analysis (Supplementary Fig. 13), the peak intensities at ~4 Å^{-1} and ~8 Å^{-1} occur due to the contributions of Fe-O (associated with single atoms) and Fe-Fe (associated with nanoparticles), respectively. These findings reveal that only the FJH-Fe-G material contained single Fe atoms and Fe nanoparticles on its surface, which is consistent with the STEM results. The extended X-ray absorption fine structure (EXAFS) fitting curve in Fig. 2h and the fitting parameters in Supplementary Table 5 demonstrate that the first peak in the shell structure is attributed to isolated Fe atoms that are coordinated with two O atoms, forming an Fe-O_2 structure.

Ensemble effect of C-FJH derived material during advanced oxidation processes. First, the importance of the interaction between FJH-Fe-G materials and PDS was highlighted by

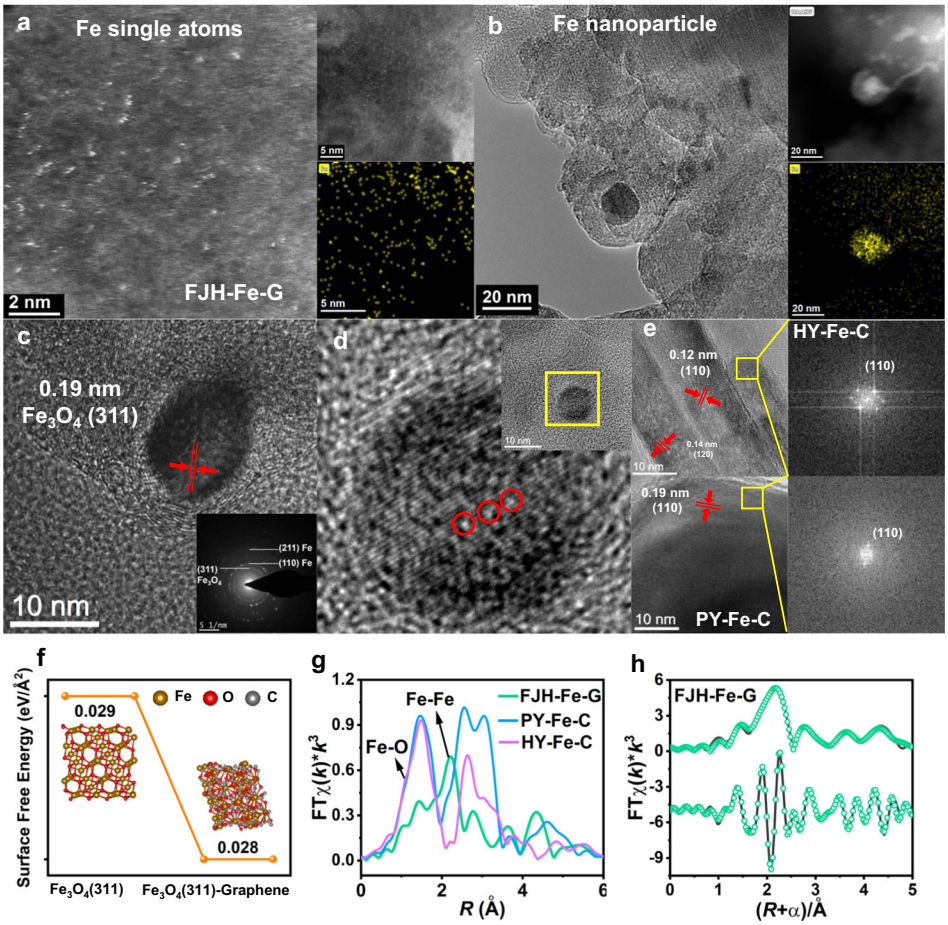

Fig. 2 Structural characterization of Fe-based Fenton-like materials. a, **b** Aberration-corrected high-angle annular dark-field scanning transmission electron microscopy (AC-HAADF-STEM) images corresponding to energy dispersive X-ray spectroscopy (EDS) elemental mapping of Fe for the C-FJH-derived material (FJH-Fe-G). **c**, **d** Transmission electron microscopy (TEM) images and selected area electron diffraction patterns of FJH-Fe-G. **e** TEM and fast Fourier transformation (FFT) images of hydrothermal coprecipitation (HY-Fe-C) and pyrolysis (PY-Fe-C) method-derived materials, respectively. **f** Calculation of the surface energy of Fe_3O_4 (311) with and without graphene as the carbon support. **g** Fourier transform (FT) of k^3-weighted Fe-EXAFS spectra of the prepared materials. **h** k^3-weighted FT-EXAFS fitting curves of FJH-Fe-G.

determining the influence of the PDS concentration (Supplementary Fig. 14). The reactive radical species generated during the catalytic reactions were subsequently tested via scavenger quenching experiments (Fig. 3a and Supplementary Fig. 15). The results indicate that the hydroxyl radicals (•OH) in liquid and the surfaces of solid[30,31] have obvious influences on CAP degradation compared to sulfate radicals (SO_4^{-}•) and singlet oxygen ($^1O_2$) radicals[32,33]. Here, 2,4,6-trimethylpyridine (TEMP) and 5,5-dimethyl-1-pyrrolidine N-oxide (DMPO) were used as spin-trapping agents for $_1O^2$ and ·OH, respectively. In Fig. 3b, the FJH-Fe-G sample can be observed with remarkable DMPO-•OH signal peaks, whereas the TMP-$^1O_2$ signal can be created in all sample solutions (Supplementary Fig. 16). The cumulative •OH concentrations during the degradation process of the FJH-Fe-G sample were an order of magnitude greater than those of the other materials (Supplementary Fig. 17). The Fe^{2+} content in the reaction solution increases over time, further verifying the crucial role of •OH radicals and Fe active sites during catalytic activation (Supplementary Fig. 18). Moreover, electron transfer is observed through cyclic voltammetry measurements. As shown in Fig. 3c, a well-defined anodic peak for the FJH-Fe-G sample emerges in a N_2-saturated solution, and the peak potential is −0.28 V, indicating the oxidation of exposed Fe active sites (e.g., $Fe^0 \rightarrow Fe^{2+} + 2e^-$). The FJH-Fe-G sample displays the smallest semicircle with the lowest charge transfer resistance (R_{ct}) value of 38 Ω after fitting (Supplementary Fig. 19), suggesting its increased electron transfer ability. Furthermore, as shown in Fig. 3d, e, the loading of single Fe atoms can modify the band structure, and the highest occupied molecular orbital (HOMO) is close to the Fermi level. The low HOMO energy level (FJH-Fe-G: 1.87 eV) indicates easier electron loss than that of other materials, and the former acts as an electron donor[34]. Additionally, the FJH-Fe-G material has a low energetic barrier for transferring electrons from the active sites and accelerates the reaction rate of •OH production due to the low work function value of 4.38 eV. This value may be attributed to the unique electronic properties of Fe nanoparticles associated with high-index facets, which synergize with Fe atoms to achieve high reactivity.

To further analyze the surface reaction process, the $S_2O_8^{2-}$ molecules are first adjusted to be adsorbed on the specific crystal planes of Fe (110) and Fe_3O_4 (311), and the atomic structure of Fe-O_2-G is constructed on graphene (Supplementary Fig. 20). The shortest adsorption distances on the Fe plane of $S_2O_8^{2-}$ were 1.84 Å (Fe-O) and 2.30 Å (Fe-S), while those on Fe_3O_4 were 2.60 Å (Fe-O) and 2.06 Å (Fe-S). The adsorption distance and energy of Fe-O_2-G were 1.92 Å and −0.63, respectively. Generally, the isolated Fe atoms on the surface have been recognized as high-efficiency active centers for catalyzing oxygen reduction[35,36]; thus, O atoms from PDS are preferentially absorbed and create Fe-O bonds.

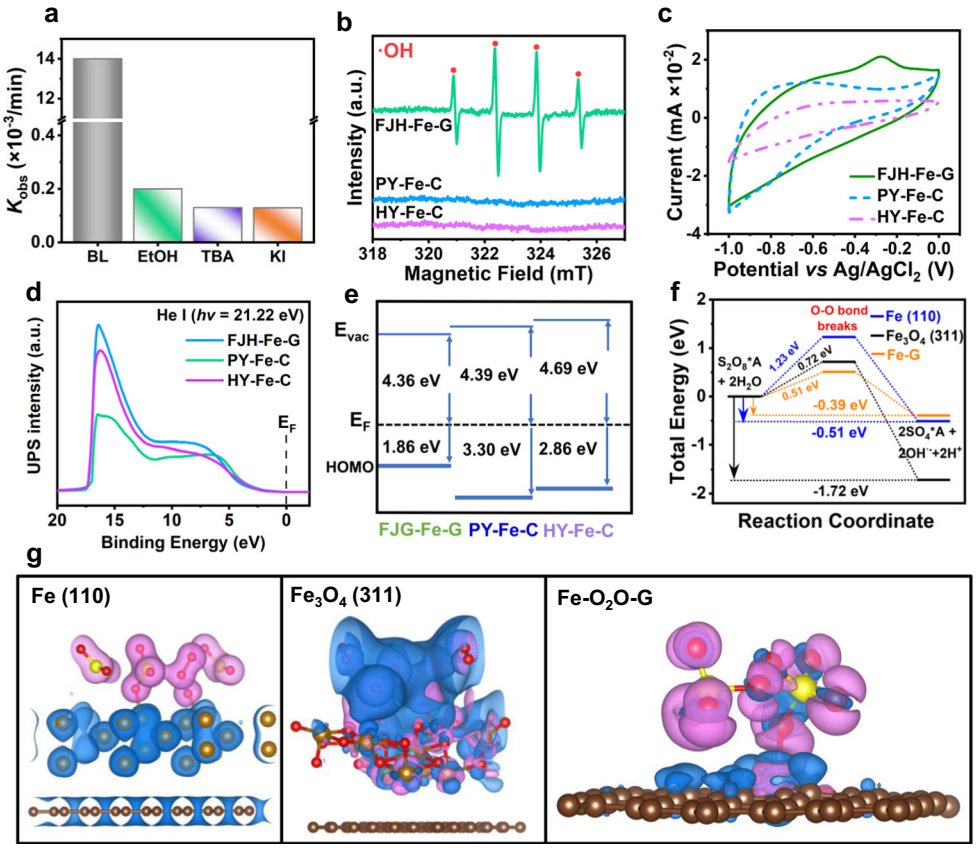

Fig. 3 Interactions between C-FJH materials and PDS. a Inhibition efficiency of different quenching agents on the basis of catalytic activity. **b** Electron paramagnetic resonance (EPR) spectra using DMPO as a trapping reagent for •OH. **c**, **d** CV curves and ultraviolet photoelectron spectroscopy (UPS) He I spectra of materials derived from various methods. **e** Workfunction and HOMO density calculated from the UPS spectra. **f** DFT calculation of the O-O bond break during •OH formation. **g** Effects of Fe-exposed active sites (the crystal planes of Fe (110) and Fe_3O_4 (311) and the atomic structure of Fe-O_2-G constructed upon graphene) on electron transfer to persulfate.

To explore the determining step of O-O bond breakage during the catalytic reaction, the possible transition structure, relative energy and activation energy were calculated. As shown in Fig. 3f, the differences in Gibbs free energy are negative, which indicates a spontaneous process in this system. According to the model of Fe-O_2-G, a low energy barrier of only 0.51 eV must be overcome during the O-O bond breakage process. After the O-O bond in the Fe_3O_4 (311) plane model is broken, a barrier of 0.72 eV is overcome, 1.72 eV of heat is released, and •OH is created. The introduction of vacancies increases the density of localized unpaired electrons, making the surface highly chemically reactive (Fig. 3g) and establishing an electron transfer channel. This system exhibits self-relay catalysis, where atomic Fe serves as the electron donor, facilitating the adsorption of $S_2O_8^{2-}$ and the formation of atomic oxygen. Adjacent nanoparticles adjusted by a high-index facet with oxygen vacancies can afford a larger electron region and improve the efficiency of electron transport. Therefore, the accumulated atomic oxygen and dissociative H^+ facilitate into •OH formation, by significantly reducing the speed barrier of rapid surface redox reactions. Furthermore, different Fe sites were simulated for CAP removal, and the results showed that (Supplementary Fig. 21), FJH-Fe-G associated with Fe atoms play a major role of active in activating PDS by decreasing the reaction energy barrier of the O-O bond breakage process. In addition, Fe^0 and Fe^{2+} (from the Fe-O structure in FJH-Fe-G) can give soluble Fe^{2+} for •OH production. The Fe_3O_4 sites showed limited degradation of CAP; according to the DFT calculations, the Fe_3O_4 sites mainly promoted electron transport during •OH production. Thus, different active sites are organized according to their functions to improve CAP removal.

Subsequently, we carried out CAP removal experiments with simulated wastewater at different pH values and containing common co-existing substances, including Cl^-, HCO_3^-, SO_4^{2-} and humic acid. As shown in Supplementary Fig. 22a, the material exhibited significant CAP degradation efficiency over a wide pH range. After 90 min of reaction, the presence of additional inorganic anions and humic acid had an insignificant effect on the removal efficiency of CAP (Supplementary Fig. 22b). The removal efficiency of CAP still reached more than 90% after 90 min. Finally, we identified the intermediates from CAP degradation by the FJH-Fe-G materials and PDS system, and the results are shown in Supplementary Fig. 23. According to previous studies[37,38], the main pathways of CAP degradation are dehydration, •OH addition, and C-C/C-N bond breakage reactions. Small molecule compounds are detected after 15 min of degradation (Supplementary Table 6); generally, these intermediates undergo further dechlorination and are oxidized to produce inorganic components, such as CO_2, H_2O, NO_3^- and Cl^-.

Effedt of electric current on optimizing C-FJH derived materials. To gain insight into the synthesis mechanism, several materials prepared with different voltages were tested for CAP degradation (Fig. 4a). The current-controlled synthesis process affected the kinetic constant of the degradation, resulting in high k_{obs} values for the sample treated with a 100 V FJH starting

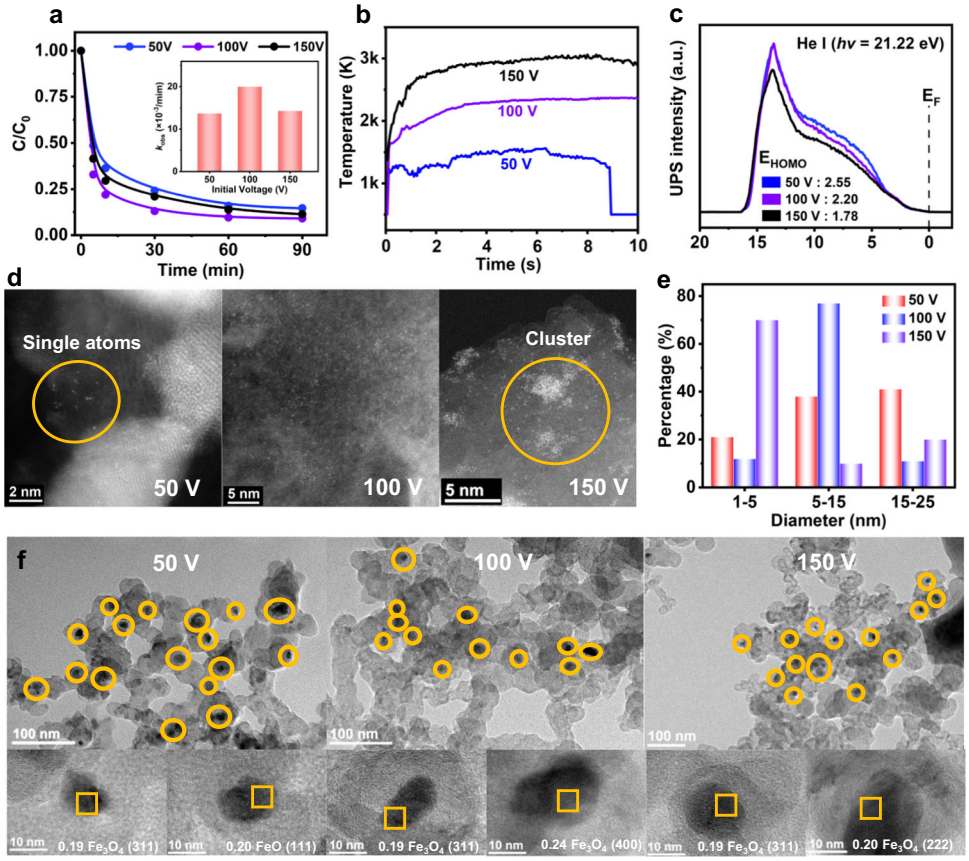

Fig. 4 C-FJH effect dominates the features of the derived materials. a CAP degradation in the PDS system by FJH-Fe-G under different initial voltage treatments. Inset pattern: k_{obs} of CAP degradation by different materials. **b** Temperature recorded during the C-FJH process. **c** UPS He I spectra of C-FJH-derived materials. **d** STEM images and corresponding elemental mapping of Fe for EDS images of the C-FJH-derived material prepared at different initial voltages. **e** Corresponding Fe nanoparticle size distribution of C-FJH-derived samples detected by high-angle annular dark-field scanning transmission electron microscopy (HAADF–STEM). **f** TEM images and nanoparticles corresponding to the facets of C-FJH-derived materials.

voltage (inset of Fig. 4a). In addition, the initial Fe dosage was determined, and a limited impact on CAP degradation was observed (Supplementary Fig. 24 and Supplementary Table 7), indicating that the initial voltage played a key role in material conditioning. During the C-FJH process, a high initial voltage could increase the energy needed to increase the reaction temperature (Fig. 4b), and a proper reaction temperature induced C-FJH features, which were beneficial for dispersing metal atoms and restraining caking by rapid thermal annealing. An increase in temperature caused thermal shock, which was beneficial for the construction of single Fe atom on the carbon matrix, leading to a decrease in E_{HOMO} to a value near the Fermi level (Fig. 4c). The STEM images show that single atoms and nanoparticles can be simultaneously obtained on the graphene support under all voltage conditions (Fig. 4d and Supplementary Fig. 25). However, at a low temperature (50 V), large Fe nanoparticles are generated instead of single atoms. Both low (50 V) and high (150 V) temperatures can lead to the superimposition of carbon layers (Supplementary Fig. 26). Low temperatures limit exfoliation, while high temperatures induce carbon polymerization reactions; finally, a high temperature decreases the degree of graphitization (Supplementary Fig. 27), hindering the distribution of active sites. A temperature reached of ~3000 K was not conducive to single-atom synthesis, and a strong interaction force was induced between atoms, causing aggregation and sintering[25,39]. Single atoms aggregated into nanoclusters (Fig. 4d), increasing the ratio of Fe nanoparticles in the range of 1–5 nm in the material treated with 150 V (Fig. 4e). According to the above analysis, the system could promote surface reactions due to enhanced adsorption by single atoms. In addition, single atoms and nanoparticles have a binary complementary effect[40]. Thus, when both of these agents were dispersed uniformly on a support material (at 100 V; Supplementary Fig. 28), they could catalyze the different steps independently and accelerate the overall reaction collectively to realize self-relay catalysis.

Additionally, the current induces an increase in initial temperature, affecting the retention facets of the Fe materials. The resultant sample could retain high-index facets, such as the (311) and (400) facets of Fe_3O_4, after 100 V treatment (Fig. 4f and Supplementary Fig. 29). The ultrahigh temperature caused by 150 V increased the rapid quenching time, leading to the recombination of low-index facets, such as (211) in Fe_3O_4 (Fig. 4f and Supplementary Fig. 29). A comparison of the materials showed that when the initial voltage was 100 V, optimization of the combination of Fe valence states resulted in more active sites ($Fe^{0/2+}$: $Fe^{total} = 0.64$, Supplementary Fig. 30) and a graphitized structure (I_D:$I_G = 0.36$, Supplementary Fig. 27). These unique characteristics were confirmed by the above analysis, which could be further adjusting the technical parameters to increase the degradation rate.

C-FJH derived materials for the deep purification of antibiotic wastewater. The abuse of antibiotic drugs that cause residues in natural water poses a serious safety risk, including antibiotic resistance in bacteria and ecosystem destruction[41,42]. Some

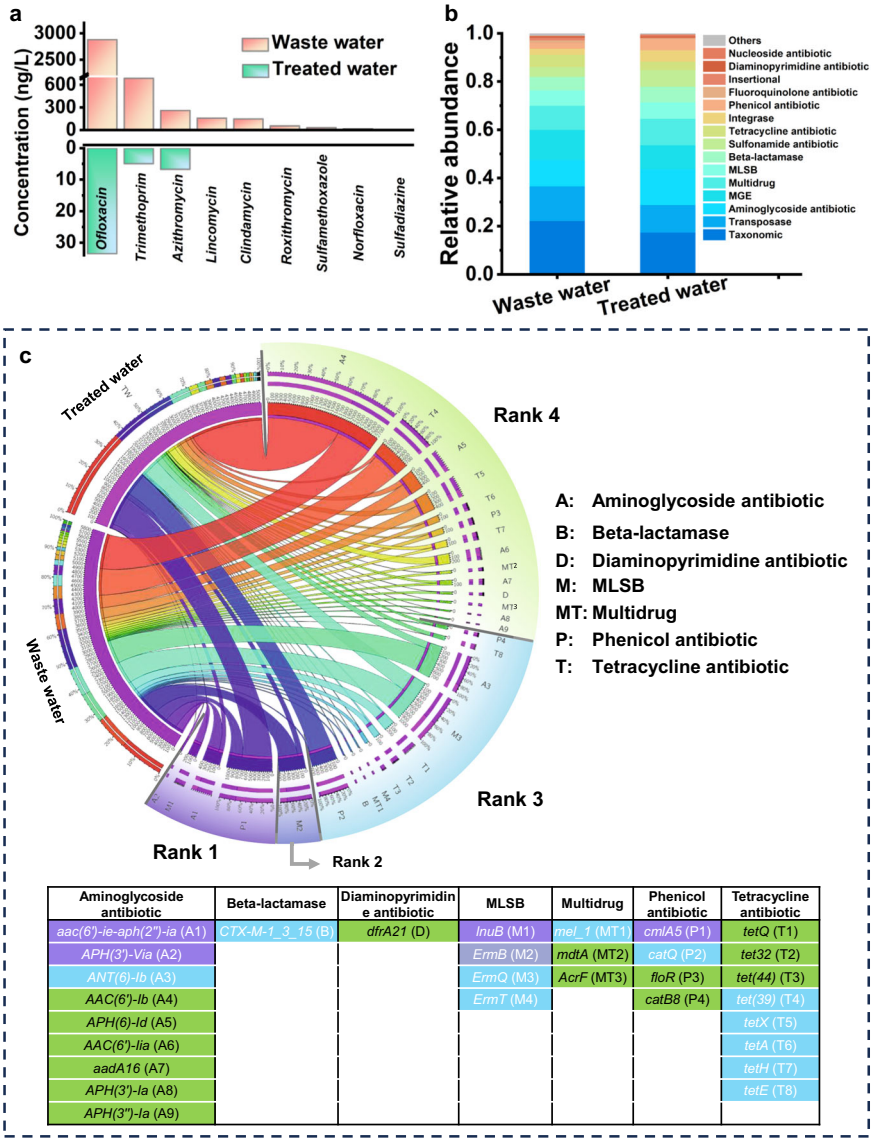

Aminoglycoside antibiotic	Beta-lactamase	Diaminopyrimidine antibiotic	MLSB	Multidrug	Phenicol antibiotic	Tetracycline antibiotic
aac(6')-ie-aph(2")-ia (A1)	*CTX-M-1_3_15* (B)	*dfrA21* (D)	*lnuB* (M1)	*mel_1* (MT1)	*cmlA5* (P1)	*tetQ* (T1)
APH(3')-Via (A2)			*ErmB* (M2)	*mdtA* (MT2)	*catQ* (P2)	*tet32* (T2)
ANT(6)-Ib (A3)			*ErmQ* (M3)	*AcrF* (MT3)	*floR* (P3)	*tet(44)* (T3)
AAC(6')-Ib (A4)			*ErmT* (M4)		*catB8* (P4)	*tet(39)* (T4)
APH(6)-Id (A5)						*tetX* (T5)
AAC(6')-Iia (A6)						*tetA* (T6)
aadA16 (A7)						*tetH* (T7)
APH(3')-Ia (A8)						*tetE* (T8)
APH(3")-Ia (A9)						

Fig. 5 Performance of C-FJH derived materials in wastewater treatment. a Antibiotic contents in the water samples. **b** Quantification of antibiotic resistance gene (ARG) abundance levels for the 15 classes detected in the water sample analysis by quantitative polymerase chain reaction (q-PCR). **c** Changes in the top 30 known high-risk ARG families.

antibiotics, such as fluoroquinolones and tetracyclines, are relatively persistent and can be resistant to degradation by conventional treatment methods. There is a need for innovative and alternative solutions to address the problem of antibiotic contamination. Thus, C-FJH-derived materials have been applied to explore the potential of applying these materials for wastewater treatment by removing antibiotics. To achieve this purpose, a wastewater sample was taken from the drain of the hospital (after wastewater treatment systems), and its characteristics were analyzed (Supplementary Table 8). Nine of the 32 antibiotics were detected in the wastewater sample with concentrations ranging between 0.03 μg/L and 2.88 μg/L (Fig. 5a). The sample mainly included certain antibiotics, such as fluoroquinolones, macrolides, and sulfonamides, based on their chemical structures. Among these antibiotics, the main risk factor for wastewater is quinolone antibacterial agents (*ofloxacin*), which are broad-spectrum antibiotics and persistent organic pollutants that usually need advanced oxidation processes for deep degradation. After degradation (sample TW, Figs. 5a), 97.4% to 100% of the detected antibiotics were removed, demonstrating the high efficiency of the FJH-Fe-G material due to a structurally induced rapid oxidation reaction. The resultant concentrations (0 ~ 33.5 ng/L) of antibiotics are much lower than acute or chronic ecotoxicity (range from 0.009 to 1500 mg/L), which has been assessed by standard ecotoxicity assays on organisms in previous studies[43].

However, exposure to antibiotics in the environment inevitably enriches antibiotic resistance genes (ARGs). Thus, for in-depth discussion of the risk of ARG transfer, high-throughput quantitative polymerase chain reaction (PCR) was used to analyze ARGs[44]. Our results revealed that the abundances of taxonomic, transposase and mobile genetic element (MGE) types related to genetic information decreased markedly (Fig. 5b and Supplementary Fig. 31), indicating that there was a decreased potential for ARG transfer in the environment. To identify the different risk levels of ARGs, we analyzed the known high-risk ARG families identified by Zhang et al. [45]. and further identified 65 ARG families in the sample that were classified as Ranks 1–4 (Supplementary Figs. 32 and 33). After calculation, most of the high-risk ARGs were related to *aminoglycoside*, *lincosamide* and phenicol antibiotics (Supplementary Table 9). According to the

top thirty most abundant ARG families (98.3% of the total), the majority of ARGs were not high risk (high risk, Rank 2: not yet present in pathogens; Rank 1: already present in pathogens). Importantly, abundances of high-risk ARGs associated with beta-lactamases and multidrugs are usually persistent even during disinfection but significantly decreased (Fig. 5c)[46]. Generally, intracellular ARGs can be released from antibiotic-resistant bacteria and spread between different microbial species through horizontal gene transfer[47], and more stringent conditions are needed for physiochemical destruction of host cells. We observed that the abundance of *cmlA5* (phenicol antibiotic), which is an efflux pump complex or subunit that confers antibiotic resistance increased[48]. This finding may be related to attack by active substances, which changes the permeability of the cell membrane, and releases free deoxyribonucleic acid (DNA) into water[49]. These findings suggest the efficiency of C-FJH materials for ARG degradation in wastewater environments, which is achieved by reducing the richness of persistent ARGs.

In conclusion, we demonstrated a facile strategy for fabricating an Fe nanomaterial with single atoms and high-index facet nanoparticles. Due to these unique characteristics, atomic Fe can significantly accelerate adsorption and cause O–O bond dissociation. Immediately, high-index facet Fe nanoparticles with oxygen vacancies can synchronously promote rapid electronic effects and surface reaction kinetics, which will intensify •OH generation during Fenton-like catalysis. In comparison to traditional methods, C-FJH-derived materials exhibit high activity for the removal of antibiotics and ARGs to achieve deep purification of actual wastewater. In this work, we provide a successful approach for enhancing catalytic kinetics and activity, which can be extended to the optimization of other materials and provide some information for the development of water treatment applications.

Materials and methods

Carbon-assisted Flash Joule heating material synthesis. To synthesize a highly efficient material with a single Fe atom and high-index facet nanoparticles, a pretreated source containing 5 wt% carbon black (Super p li, Lizhiyuan Co., Ltd., China) was treated as a conductive material by using the C-FJH method (Supplementary Fig. 1). Briefly, 0.1 g of sample was compressed with copper electrodes in a quartz tube to minimize the sample resistance to ~100 Ω. Beforehand, the sample was mixed with carbon support (biochar) and $Fe(NO_3)_3{\cdot}9H_2O$ (Fe^{3+}: 0.0025–0.015 mol/g C) in deionized water and then dried for further use. Different Fe-based materials were synthesized by controlling the C-FJH parameters, including the current-related external resistance (5–30 Ω) and reaction time (10 s), under mild vacuum conditions. To further explain the reaction phenomenon of the C-FJH process, the voltage and current were recorded by an oscilloscope (RIGOL, DS1104Z Plus).

Mechanism of carbon-assisted Flash Joule heating derived material in pollutant degradation. The oxidative degradation of organic pollutants by activating PDS was performed in a stirred 50 mL conical flask at room temperature. A typical experimental suspension contained 0.5 g/L material and 80 mg/L CAP. The experiment was initiated after adding different material suspensions to solutions with/without PDS at various concentrations. Reaction aliquots were periodically taken and filtered through a membrane (0.22 μm) to remove the solid materials for analysis. The residual concentrations of CAP were analyzed by using a high-performance liquid chromatograph (Agilent, USA) at a wavelength of 278 nm. An Agilent Eclipse C18 column (3.0 mm × 150 mm, 1.8 μm) was used for separation. The injection volume was 5.0 μL, and methanol (70% in deionized water) was selected as the mobile phase at a flow rate of 1 mL/min. All degradation tests were conducted in duplicate, and the mean values with standard deviation are presented. The detailed experimental conditions and analytical methods are presented in the *SI Appendix*.

Carbon-assisted Flash Joule heating derived material in actual wastewater treatment. For the environmental testing of materials, wastewater samples were collected from a hospital in Guangzhou, China, in August 2022. The characteristics of the samples are listed in Supplementary Table 8. Degradation tests were conducted in the FJH-Fe-G material and PDS system for comparison. Typically, a 1-L wastewater sample containing 0.5 mg/L FJH-Fe-G and 5 mmol/L PDS was continuously shaken in the reactor at 150 rpm. The water sample was filtered through a 0.45-μm membrane filter, and the membrane was preserved for ARG analysis. High-molecular-weight community DNA was extracted by the freeze-grinding, sodium dodecyl sulfate (SDS)-based method, and it was purified using a low-melting agarose gel followed by phenol extraction[50]. DNA concentration and quality were determined with a NanoDrop ND-1000 spectrophotometer (NanoDrop Technologies Inc.). SmartChip Real-Time PCR (Warfergen) was used to determine the compositions of ARGs in water samples[44,51]. In this study, we used 296 primer sets targeting 285 ARGs and one 16 S ribosomal ribonucleic acid (rRNA) gene conferring resistance to major antibiotic classes. The experimental details are shown in SI.

Primer sets were grouped into 11 resistance gene class by subjecting all primer sets BLAST tool in the National Center for Biotechnology Information. The obtained PCR products were verified manually by BLAST searches. The health risks of ARGs were classified according to the risk ranking framework based on the assessment of three criteria by Zhang's study[45], and ARGs were further categorized into four ranks (Supplementary Fig. 32).

Data availability

Details on the sample characteristics and degradation experiments are included in the *SI Appendix*. DFT calculations were performed by a Vienna ab initio simulation package (VASP) using the projector augmented wave (PAW) method, which is shown in the *SI Appendix*.

Received: 3 August 2023; Accepted: 9 January 2024;
Published online: 25 January 2024

References

1. Cheng, M. et al. Metal-organic frameworks for highly efficient heterogeneous Fenton-like catalysis. *Coordin. Chem. Rev.* **368**, 80–92 (2018).
2. Wang, J. H. et al. An ultrafast and facile nondestructive strategy to convert various inefficient commercial nanocarbons to highly active Fenton-like catalysts. *Proc. Natl Acad. Sci. USA* **119**, e2114138119 (2022).
3. Yang, Z. C. et al. Singlet oxygen mediated iron-based Fenton-like catalysis under nanoconfinement. *Proc. Natl Acad. Sci. USA* **116**, 6659–6664 (2019).
4. Shang, Y. N. et al. Single-atom catalysis in advanced oxidation processes for environmental remediation. *Chem. Soc. Rev.* **50**, 5281–5322 (2021).
5. Xiao, C. et al. High-index-facet- and high-surface-energy nanocrystals of metals and metal oxides as highly efficient catalysts. *Joule* **4**, 2562–2598 (2020).
6. Chen, Z. et al. Single-atom Mo–Co catalyst with low biotoxicity for sustainable degradation of high-ionization-potential organic pollutants. *Proc. Natl Acad. Sci. USA* **120**, e2305933120 (2023).
7. Shen, Q. K. et al. Breaking the activity limitation of iridium single-atom catalyst in hydrogenation of quinoline with synergistic nanoparticles catalysis. *Nano Res.* **15**, 5024–5031 (2022).
8. Jiang, W. J. et al. Understanding the high activity of fe-n-c electrocatalysts in oxygen reduction: Fe/Fe_3C Nanoparticles boost the activity of Fe-N-x. *J. Am. Chem. Soc.* **138**, 3570–3578 (2016).

9. Ma, Z. M. et al. Coexistence of Fe nanoclusters boosting fe single atoms to generate singlet oxygen for efficient aerobic oxidation of primary amines to imines. *ACS Catal.* **12**, 5595–5604 (2022).
10. Wang, Z. et al. Understanding the synergistic effects of cobalt single atoms and small nanoparticles: enhancing oxygen reduction reaction catalytic activity and stability for Zinc-Air batteries. *Adv. Funct. Mater.* **31**, 2104735 (2021).
11. Zong, Y. et al. Enhanced oxidation of organic contaminants by iron(II)-activated periodate: the significance of high-valent iron-Oxo species. *Environ. Sci. Technol.* **55**, 7634–7642 (2021).
12. Wang, S. Z. et al. Peroxymonosulfate activation by Fe-Co-O-codoped graphite carbon nitride for degradation of sulfamethoxazole. *Environ. Sci. Technol.* **54**, 10361–10369 (2020).
13. Liu, L. C. & Corma, A. Metal catalysts for heterogeneous catalysis: from single atoms to nanoclusters and nanoparticles. *Chem. Rev.* **118**, 4981–5079 (2018).
14. Zhao, J. et al. Direct in situ observations of single Fe atom catalytic processes and anomalous diffusion at graphene edges. *Proc. Natl Acad. Sci. USA* **111**, 15641–15646 (2014).
15. Qiu, H. J. et al. Nanoporous graphene with single-atom nickel dopants: an efficient and stable catalyst for electrochemical hydrogen production. *Angew. Chem. Int. Edit.* **54**, 14031–14035 (2015).
16. Shan, J. Q. et al. Metal-metal interactions in correlated single-atom catalysts. *Sci. Adv.* **8**, eabo0762 (2022).
17. Shen, B. et al. Crystal structure engineering in multimetallic high-index facet nanocatalysts. *Proc. Natl Acad. Sci. USA* **118**, e2105722118 (2021).
18. Yao, Y. et al. Mn-Co dual sites relay activation of peroxymonosulfate for accelerated decontamination. *Appl. Catal. B: Environ.* **330**, 122656 (2023).
19. Luo X. et al. Relay catalysis of multi-sites promotes oxygen reduction reaction. *Adv. Funct. Mater.*, 2215021 (2023).
20. Sun, J. F. et al. Isolated single atoms anchored on N-Doped carbon materials as a highly efficient catalyst for electrochemical and organic reactions. *ACS Sustain Chem Eng.* **8**, 14630–14656 (2020).
21. Luong, D. X. et al. Gram-scale bottom-up flash graphene synthesis. *Nature* **577**, 647–651 (2020).
22. Chen, W. Y. et al. Millisecond conversion of metastable 2D materials by flash joule heating. *Acs Nano* **15**, 1282–1290 (2021).
23. Chen, F. J. et al. High-temperature atomic mixing toward well-dispersed bimetallic electrocatalysts. *Adv Energy Mater.* **8**, 1800466 (2018).
24. Yao, Y. G. et al. Carbothermal shock synthesis of high-entropy-alloy nanoparticles. *Science* **359**, 1489–1494 (2018).
25. Wei, S. J. et al. Direct observation of noble metal nanoparticles transforming to thermally stable single atoms. *Nat. Nanotechnol.* **13**, 856–861 (2018).
26. Algozeeb, W. A. et al. Flash graphene from plastic waste. *ACS Nano* **14**, 15595–15604 (2020).
27. Wang, J. D. et al. Approach and coalescence of gold nanoparticles driven by surface thermodynamic fluctuations and atomic interaction forces. *ACS Nano* **10**, 2893–2902 (2016).
28. Liu, X. Y. et al. Switching of radical and nonradical pathways through the surface defects of Fe_3O_4/MoOxSy in a Fenton-like reaction. *Sci. Bull.* **68**, 603–612 (2023).
29. Arcon, I. et al. XANES analysis of Fe valence in iron gall inks. *X-Ray Spectrom* **36**, 199–205 (2007).
30. Yu, G. F. et al. Reactive oxygen species and catalytic active sites in heterogeneous catalytic ozonation for water purification. *Environ. Sci. Technol.* **54**, 5931–5946 (2020).
31. Yan, Q. Y. et al. Constructing an acidic microenvironment by MoS_2 in heterogeneous Fenton reaction for pollutant control. *Angew. Chem. Int. Edit* **60**, 17155–17163 (2021).
32. Zhang, J. & Nosaka, Y. Photocatalytic oxidation mechanism of methanol and the other reactants in irradiated TiO_2 aqueous suspension investigated by OH radical detection. *Appl. Catal. B-Environ.* **166**, 32–36 (2015).
33. Yang, L. X. et al. Fe single-atom catalyst for efficient and rapid Fenton-like degradation of organics and disinfection against bacteria. *Small* **18**, 2104941 (2022).
34. Yang, J. R. et al. Electronic metal-support interaction of single-atom catalysts and applications in electrocatalysis. *Adv. Mater.* **32**, 2003300 (2020).
35. Wang, X. Q. et al. Review of metal catalysts for oxygen reduction reaction: from nanoscale engineering to atomic design. *Chem-Us* **5**, 1486–1511 (2019).
36. Cao, P. K. et al. High-efficiency electrocatalysis of molecular oxygen toward hydroxyl radicals enabled by an atomically dispersed iron catalyst. *Environ. Sci. Technol.* **54**, 12662–12672 (2020).
37. Dong, H. Y. et al. Degradation of chloramphenicol by UV/chlorine treatment: Kinetics, mechanism and enhanced formation of halonitromethanes. *Water Res.* **121**, 178–185 (2017).
38. Zhang, J. J. et al. Ferrate modified carbon felt as excellent heterogeneous electro-Fenton cathode for chloramphenicol degradation. *Water Res.* **227**, 119324 (2022).
39. Jones, J. et al. Thermally stable single-atom platinum-on-ceria catalysts via atom trapping. *Science* **353**, 150–154 (2016).
40. Zhang, L. et al. Nurturing the marriages of single atoms with atomic clusters and nanoparticles for better heterogeneous electrocatalysis. *Interdisciplinary Mater.* **1**, 51–87 (2022).
41. Zhang, Z. Y. et al. Assessment of global health risk of antibiotic resistance genes. *Nat. Commun.* **13**, 1553 (2022).
42. Chng, K. R. et al. Cartography of opportunistic pathogens and antibiotic resistance genes in a tertiary hospital environment. *Nat. Med.* **26**, 941–951 (2020).
43. Carvalho, I. T. & Santos, L. Antibiotics in the aquatic environments: a review of the European scenario. *Environ. Int.* **94**, 736–757 (2016).
44. Zhu, D. et al. Effects of trophic level and land use on the variation of animal antibiotic resistome in the soil food web. *Environ. Sci. Technol.* **56**, 14937–14947 (2022).
45. Zhang, A. N. et al. An omics-based framework for assessing the health risk of antimicrobial resistance genes. *Nat. Commun.* **12**, 4765 (2021).
46. Jia, S. Y. et al. Metagenomic profiling of antibiotic resistance genes and their associations with bacterial community during multiple disinfection regimes in a full-scale drinking water treatment plant. *Water Res.* **176**, 115721 (2020).
47. Karkman, A. et al. Antibiotic-resistance genes in waste water. *Trends Microbiol.* **26**, 220–228 (2018).
48. Porse, A. et al. Dominant resistance and negative epistasis can limit the co-selection of de novo resistance mutations and antibiotic resistance genes. *Nat. Commun.* **11**, 1199 (2020).
49. Zhang, S. et al. Chlorine disinfection facilitates natural transformation through ROS-mediated oxidative stress. *ISME J.* **15**, 2969–2985 (2021).
50. Zhu, Y. G. et al. Diverse and abundant antibiotic resistance genes in Chinese swine farms. *Proc. Natl Acad. Sci. USA* **110**, 3435–3440 (2013).
51. Zhao, Y. et al. AsChip: a high-throughput qPCR chip for comprehensive profiling of genes linked to microbial cycling of arsenic. *Environ. Sci. Technol.* **53**, 798–807 (2019).

Acknowledgements

This work was supported by the National Natural Science Foundation of China (No. 42207519) and GDAS' Project of Science and Technology Development (2022GDASZH-2022010105, 2020GDASYL-20200101002).

Author contributions

J.W.L. and X.D.Z. conceived and designed the experiments, J.W.L., F.B.Y., C.J., C.L., and X.D.Z. performed the experiments; J.W.L., F.B.Y., and X.D.Z. analysed the data; Q.Z., X.L.Z., F.C.W., and X.D.Z. given methodological guidance; J.W.L., X.D.Z., and X.L.Z. wrote the paper.

Competing interests

The authors declare no competing interests.

Additional information

Supplementary information The online version contains supplementary material available at https://doi.org/10.1038/s43246-024-00446-y.

Correspondence and requests for materials should be addressed to Xiangdong Zhu, Xiaoli Zhao or Fengchang Wu.

Peer review information *Communications Materials* thanks the anonymous reviewers for their contribution to the peer review of this work. Primary Handling Editors: Jet-Sing Lee. A peer review file is available.